

Characteristics of REE enrichments in the weathered granitic crust, Toboali, South Bangka: Possibility for ion adsorption-type REE mineralization

Yusuf Zaki Agung^{1,2}  | Yasushi Watanabe²  | Armin Tampubolon³ |
Asep Bahtiar Purnama⁴ | Mega Fatimah Rosana¹ 

¹Faculty of Geological Engineering,
Padjadjaran University, Bandung,
Indonesia

²Graduate School of International
Resource Science, Akita University, Akita,
Japan

³National Research and Innovation
Agency, Bandung, Indonesia

⁴Research and Development Center for
Mineral and Coal Technology, Bandung,
Indonesia

Correspondence

Yusuf Zaki Agung, Faculty of Geological
Engineering, Padjadjaran University,
Dipati Ukur No. 35, Lebakgede, Coblong
District, Bandung, Jawa Barat 40132,
Indonesia.

Email: yzakiagung@gmail.com

Yasushi Watanabe, Institution: Graduate
School of International Resource Sciences,
Akita University, 1-1 Tegatagakuen-
machi, Akita City 010-8502, Japan.

E-mail: y-watanabe@gipc.akita-u.ac.jp

Mega Fatimah Rosana, PhD Faculty of
Geological Engineering, Padjadjaran
University, Dipati Ukur No. 35,
Lebakgede, Coblong District, Bandung
City 40132, Indonesia.

E-mail: mega.fatimah.rosana@unpad.ac.id

Abstract

This study investigates the characteristics and fractionation of rare earth elements (REEs) in the weathered products of granite from South Bangka, Indonesia. Samples were collected from two drill holes (TBKP-30 and TBKP-38) at depths ranging from 0.5 to 18 m. Analytical methods, including X-ray diffraction (XRD), X-ray fluorescence (XRF), inductively coupled plasma mass spectrometry (ICP-MS), and scanning electron microscopy (SEM-EDS), were used to examine mineral compositions and REE distribution. The parent granite is an S-type biotite granite with total REE concentrations between 1081 and 1279 ppm. The dominant REE-bearing minerals are REE-fluorocarbonates (synchysite, parisite) and REE-phosphates (apatite, monazite, xenotime), accompanied by REE-silicates (allanite, thorite, zircon). Fluorocarbonates (synchysite, parisite) occur filling grain boundaries of the parental granite, suggesting later overprinting. Monazite, xenotime, and zircon were identified as part of the crystal lattice of residual minerals in both weathered profiles. TBKP-30, has significantly depleted in REEs with high intensity degree of weathering and the occurrence of gibbsite minerals. TBKP-38, has cerium enrichment in the lower profile, caused by the fixation into cerianite and/or it is incorporation with Fe-Mn hydr(oxides) along with the occurrence of kaolinite minerals. This study highlights the patterns of REE enrichment as a potential indicator of weathering intensity, providing insights crucial for the exploration of REE deposits and the development of sustainable extraction methods.

KEYWORDS

adsorption, Ce-anomaly, Indonesia, laterite, REE mineralization, weathering

1 | INTRODUCTION

Rare earth elements (REEs) recently become more valuable due to the limited sources available. These elements have critical importance in various industries such as

fluid catalytic cracking, magnets, and phosphorus, essential components in various high-tech and green technologies. REE is a group of 17 elements that include lanthanides, scandium, and yttrium on the periodic table, as defined by the International Union of Pure and

Applied Chemistry (IUPAC). REEs can be divided into two groups: light REEs (LREE: La-Eu) and heavy REEs (HREE: Ga-Lu) based on mineral crystallography (Miyawaki & Nakai, 1996). Scandium and yttrium are also classified into REEs due to their similar chemical properties and found in the same ore source as lanthanides (Balaram, 2019; Chen, 2011; Liu et al., 2023; Voncken, 2016). However, it is important to note that the geochemical behavior of scandium is distinct from that of the lanthanides due to its significantly smaller ionic radius. This difference results in scandium being more concentrated in mafic rocks, in contrast to the typical enrichment of lanthanides in felsic rocks (Sager & Wiche, 2024; Teitler et al., 2019).

REEs are categorized as critical metals since they are extensively utilized in modern and green technology (U.S. Department of Energy, 2023). In particular, dysprosium and terbium, two of HREEs, which are indispensable for the production of Nd-Fe-B magnets, are regarded to be most critical, because these elements have been exclusively produced from ion adsorption-type deposits in southern China. This deposit type forms by adsorption of REEs by clay minerals, which are the products of weathering of felsic volcanic and plutonic rocks under semi-tropical climate environments (Sanematsu & Watanabe, 2016). Tin granites are regarded as a preferential source of HREEs for ion adsorption type deposits, because HREEs become concentrated similar to tin in the highly fractionated granites. This concentration occurs due to the increased incompatibility of HREEs and tin in the residual melt during the late stages of magmatic differentiation. As granitic magmas evolve and fractionate, elements that are incompatible in the early-formed minerals, such as HREEs and tin, remain in the melt and become progressively enriched. This leads to their concentration in the highly evolved granitic phases (Ishihara & Murakami, 2006).

Indonesia is located in the southern end of the Southeast Asia Tin Belt, which extends for 2800 km from Myanmar and Thailand to Peninsular Malaysia and the Indonesia Tin Islands (Schwartz et al., 1995). Indonesia has a tropical climate characterized by high temperature, humidity, and high precipitation, which leads to the formation of a diverse range of weathering products. Despite this potential, there has been limited research on the characteristics of REE mineralization in the region, especially in the context of tropical weathering processes that can concentrate REEs in the regolith. Understanding these processes is crucial for guiding exploration and extraction efforts. This study, therefore, seeks to investigate the type and characteristics of REE mineralization in the Klabat granite weathering profile in Bangka Island. By providing mineralogical and geochemical

analyses, this research aims to contribute valuable insights into the REE potential of this region, supporting future exploration and sustainable resource management.

2 | GEOLOGICAL SETTINGS

Southeast Asia's granite pluton was divided into Eastern, Main Range, and Western granite provinces. Bangka Island is a part of the Eastern and Main granite province and is typically characterized by the distribution of biotite-hornblende monzogranite of post-collision and S/I-types granite (Cobbing, 2005; Ng et al., 2017). The Klabat Plutonic Complex is located in the southern end of Bangka Island (Figure 1a). The complex occurs as an intrusive body in the Tanjunggending Formation, which consists of alternating beds of sandstone and mudstone (Oktaviani et al., 2021). The Klabat Complex, about 15 km by 10 km in size, consists of granodiorite, granite, adamellite, diorite and quartz with aplite and pegmatite dikes (Oktaviani et al., 2021). Ng et al. (2017) reported an U-Pb zircon age of 221.1 ± 2.0 Ma for the granite in the complex. This plutonic complex is classified into those of the Main Range Province on the basis of their S-type, peraluminous chemical signatures (Ng et al., 2017; Wang et al., 2020). Oktaviani et al. (2021) reported tin mineralization represented by cassiterite in quartz stockwork in metasomatic greisen parts of the complex. Nugraheni et al. (2020) described REEs minerals such as allanite, xenotime and monazite in hornblende-biotite granite in the complex. The surface part of the plutonic rocks is heavily weathered, forming a ~50 m thick weathering profile above the fresh rocks (Figure 1b).

3 | METHODOLOGY

3.1 | Sample preparation

A weathering profile samples were obtained from the two drill holes (TBKP-30, TBKP-38) conducted by Center for Mineral Coal and Geothermal Resources, Geological Agency, Ministry of Energy and Mineral Resources, Bandung (Figure 1b). The samples were collected from non-exposed surface profile with 15-m and 18-m thick regolith using a gouge auger at a depth of 1 m from ground level. The samples were mixed for a meter to 4-m intervals. The raw samples have different shades, from brownish, reddish, and yellowish, depending on the depth (Figure 2). The samples are brittle and have no visible minerals with naked eyes. During the

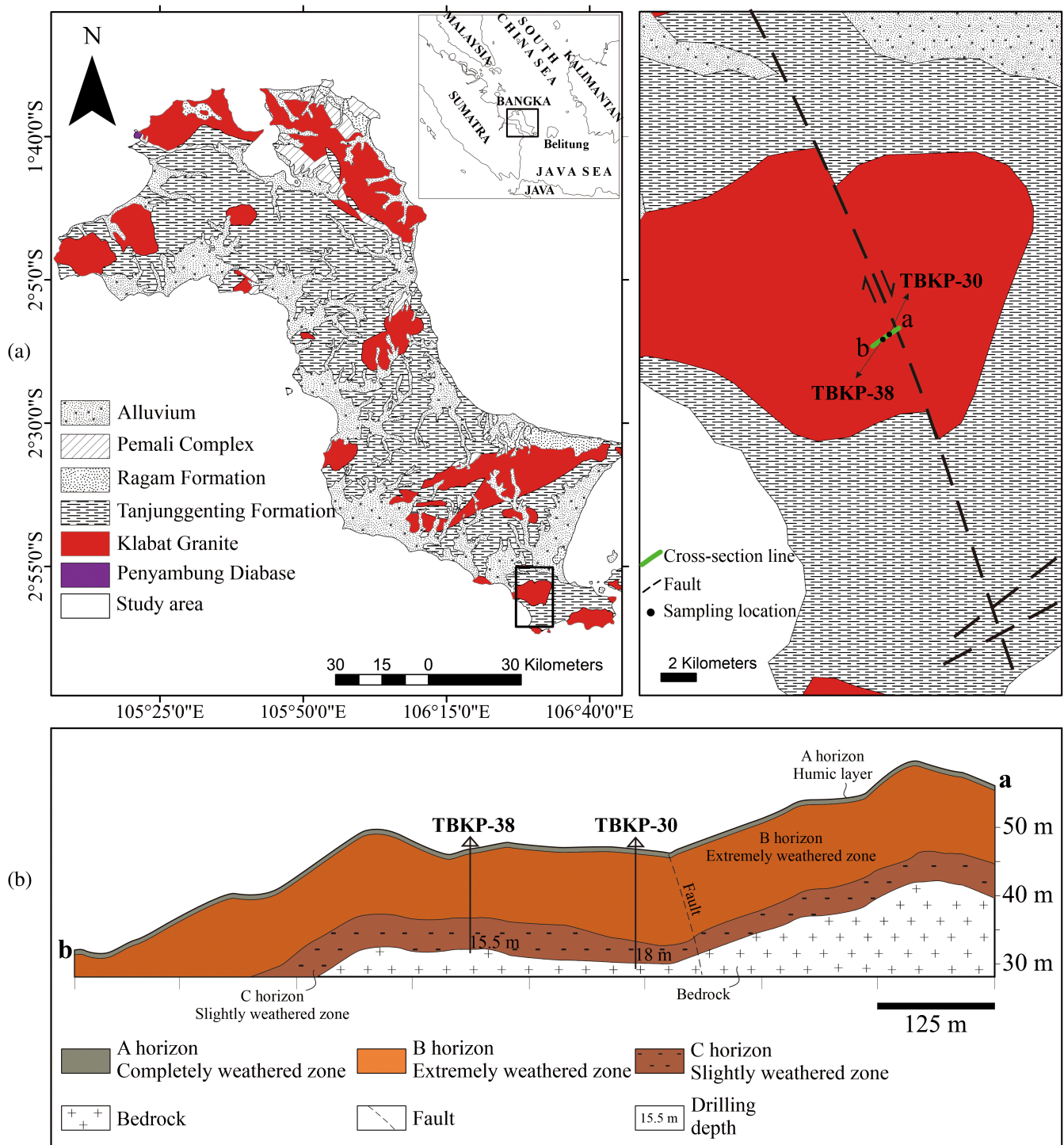


FIGURE 1 (a) Simplified geological map of Bangka Island and the study area modified after Supandjono et al. (1995). (b) A representative cross-section a and b displaying the location of the studied profiles.

characterization analysis stage, the samples were homogeneously divided through coning and quartering. Each sample was split into four almost-equal parts, combined with two opposing parts as a representative sample. Fresh rock samples were also collected from the bottom of the drill holes (Figures 2 and 3).

3.2 | Microscopic observation

The samples were made into thin sections and polished sections. The fresh rock samples were made into thin sections; the weathered samples were made into polished sections. These thin and polished sections were observed

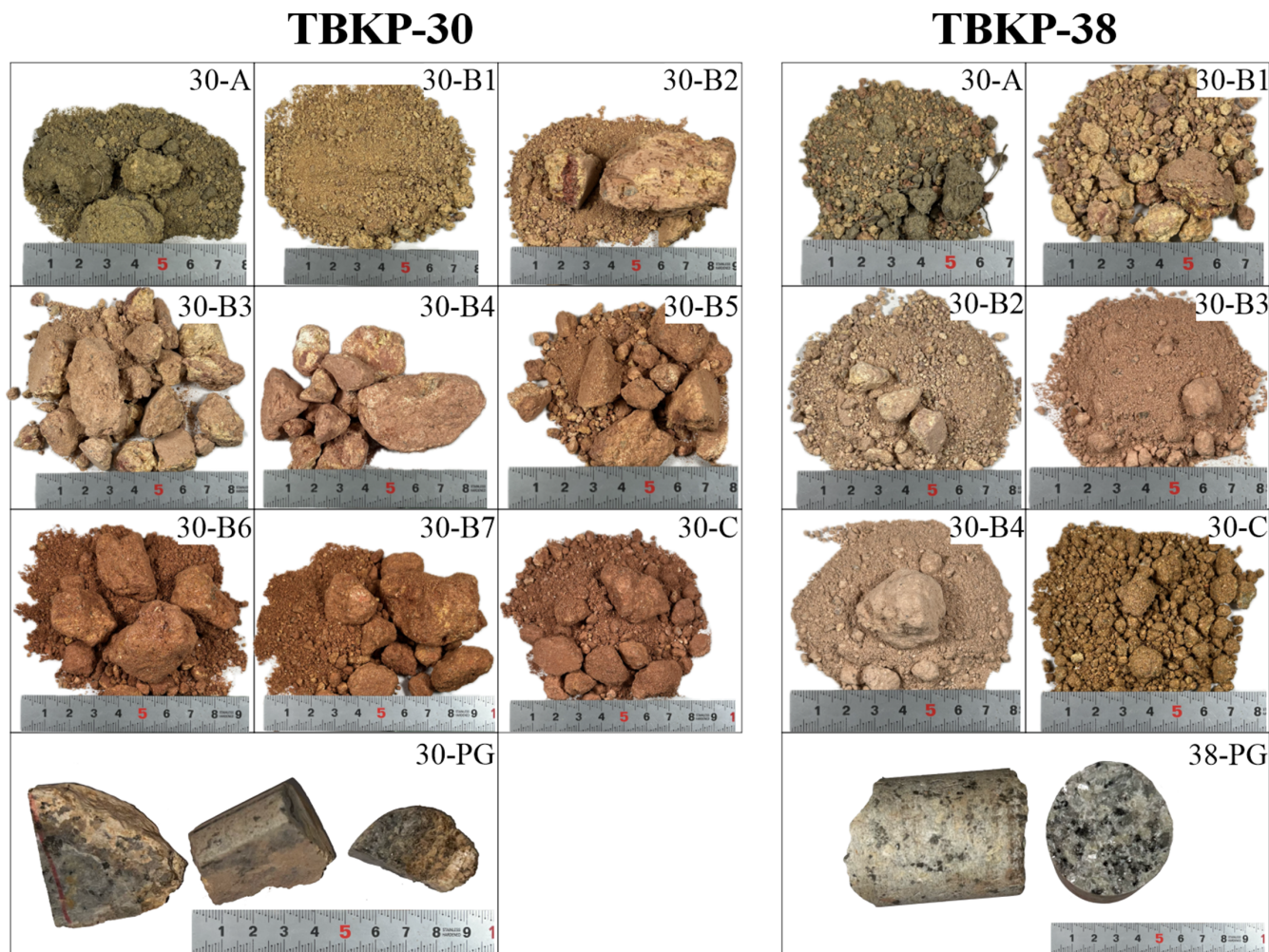


FIGURE 2 Weathered granite and parent granite samples of TBKP-30 and TBKP-38.

by optical microscope Nikon Eclipse LV100N. Modal mineralogical abundance was quantified through the point counting method, which involved the examination of 1000 points in each sample using J-Microvision software. These sections were also observed by Scanning Electron Microscopy with Energy Dispersive X-ray Spectroscopy (SEM-EDS) (JEOL JSM-6610) to analyze the chemical compositions of REE-bearing minerals in the samples. These observations were conducted at Akita University, Japan.

3.3 | Mineral phase and lithogeochemistry

X-ray diffraction patterns were utilized to identify the clay minerals by analyzing their peak position, intensity, and shape at Akita University (Rigaku Multi-Flex X-ray Diffractometer). Bragg's law was used to determine the position of the peaks, which establishes a relationship

between the wavelength of X-rays, the distance between atoms in the crystal lattice, and the angle of incidence. The peaks were mostly observed in the range of $2\theta = 40^\circ$ or less.

X-ray fluorescence (XRF) and inductively coupled plasma mass spectrometry (ICP-MS) techniques were used to analyze major and trace elements of the samples. Sample powders were prepared by using an iron mortar and pulverized using an agate mortar at Akita University. Both analyses were carried out at Activation Laboratories Ltd., Canada by a lithium metaborate/tetraborate fusion method (4 Litho package) (Figure 4).

4 | RESULTS

4.1 | Petrography of parent granite

The bottom fresh rock collected from the surveyed area is classified into granite based on the modal abundance of

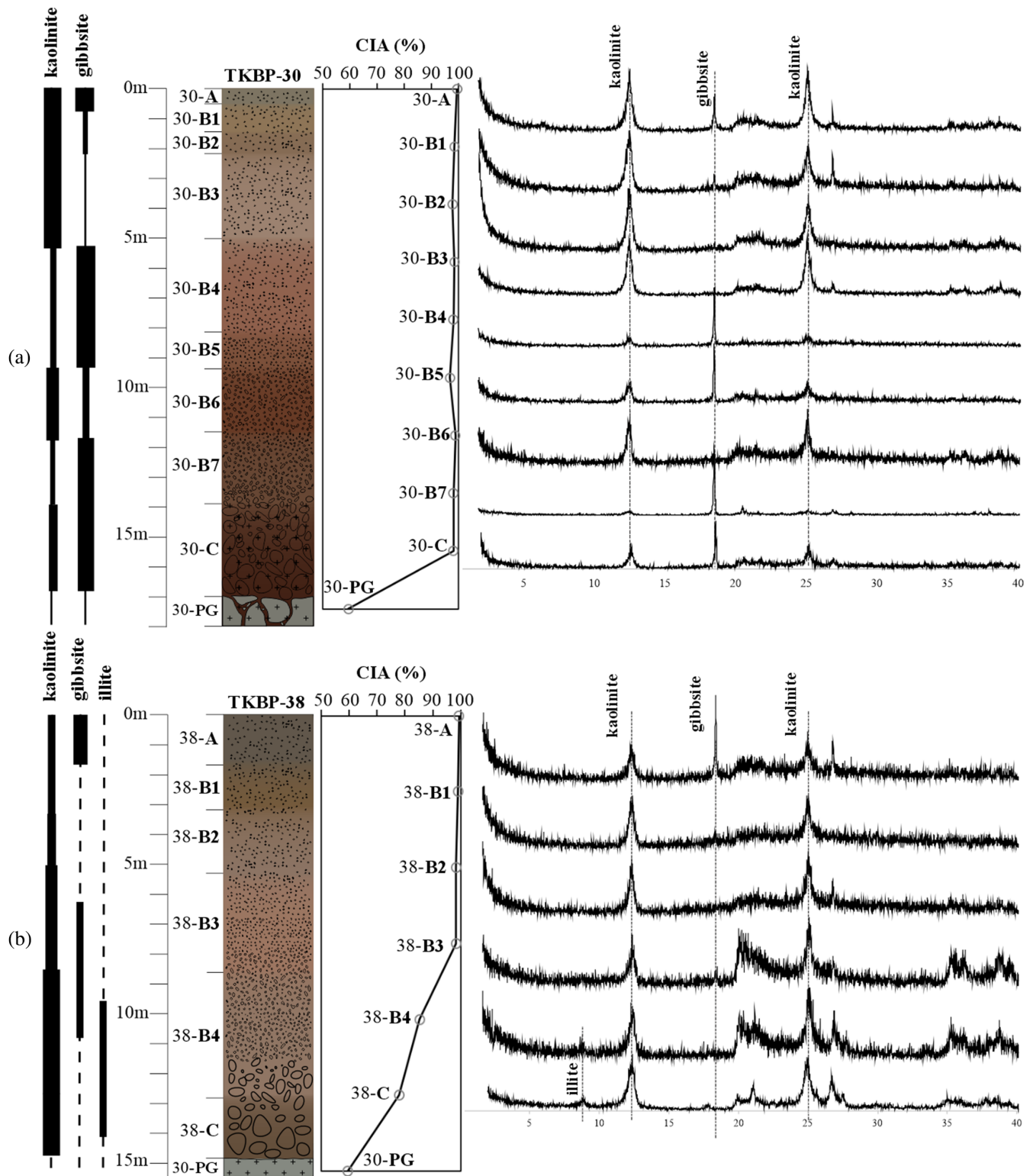


FIGURE 3 Schematic profile section of the studied weathering profile (the colors in the profile section represent the color of the samples). (a) TBKP-30 and (b) TBKP-38 on Klabat granite in South Bangka. Samples were divided from A horizon, B horizon, C horizon, and parent granite (PG). Bars indicate relative abundances of dominant clay minerals Chemical Alteration Index (CIA) is from Nesbitt (1979).

quartz, alkali feldspar, and plagioclase from the International Union of Geological Sciences (IUGS) classification (Figure 5). The modal mineralogy of sample TBKP-30

consists of 64% orthoclase, 6% plagioclase, 14% quartz, and 4% biotite. Zircon, apatite, and ilmenite occur as accessory minerals, each present in amounts less than 1%

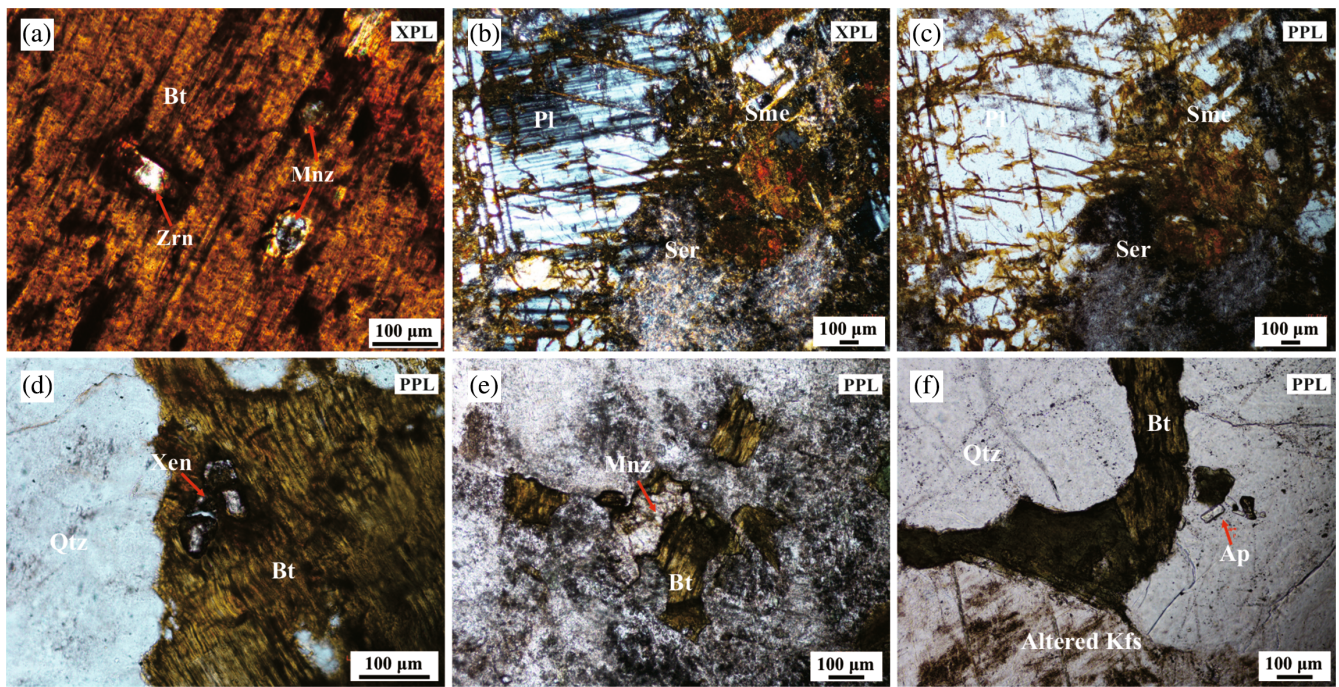


FIGURE 4 Photomicrographs of sample TBKP-30 PG: (a) Biotite-hosted zircon and monazite, with metamict halo of hematite. (b) Plagioclase altered into iron-rich smectite, (c) K-feldspar altered into sericite, (d) Quartz and biotite-hosted xenotime, (e) Monazite with biotite and (f) Quartz-hosted apatite. Ap, apatite; Bt, biotite; Kao, kaolinite; Kfs, k-feldspar; Mnz, monazite; Ms., muscovite; Pl, plagioclase; Qtz, quartz; Sme, smectite; Ser, sericite; Xt, xenotime; Zrn, zircon.

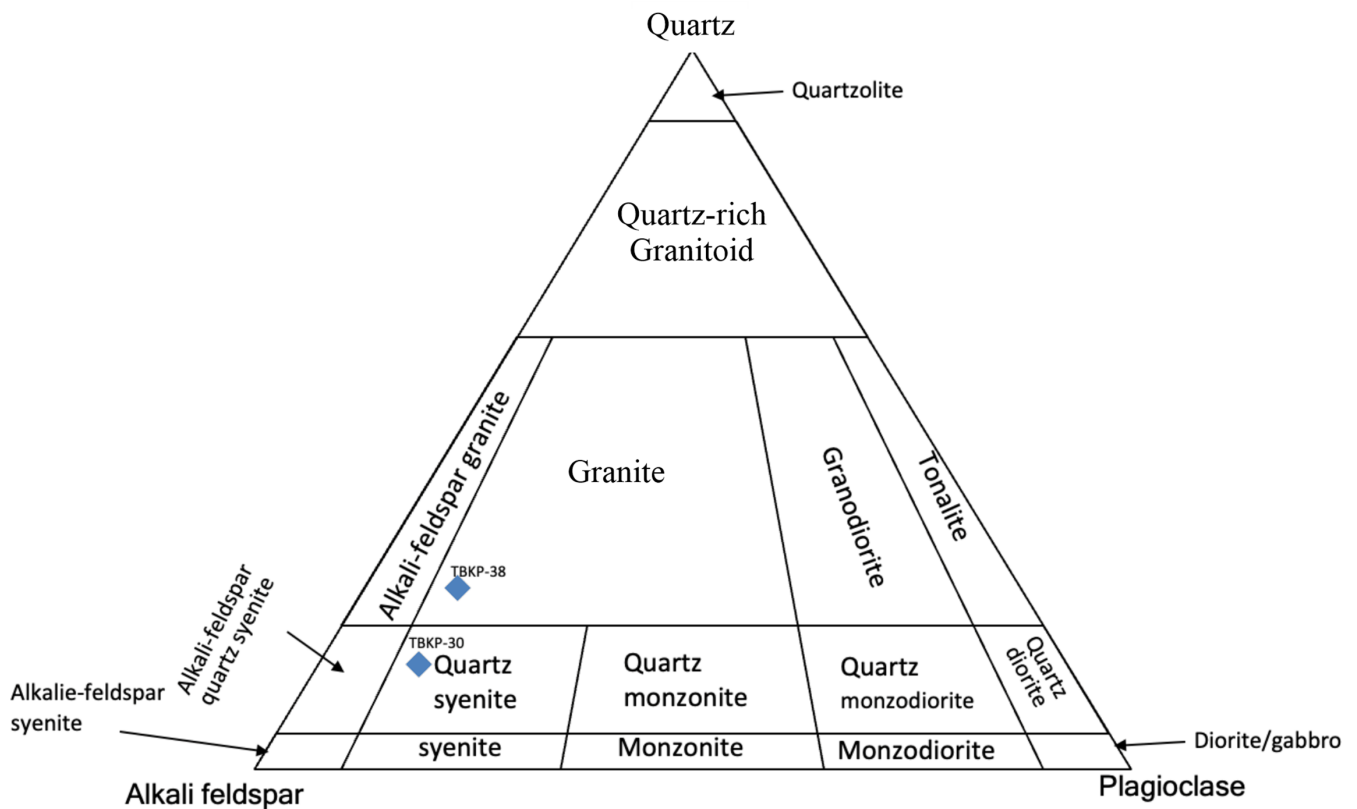


FIGURE 5 Modal composition in parent granite (TBKP-30 and TBKP38).

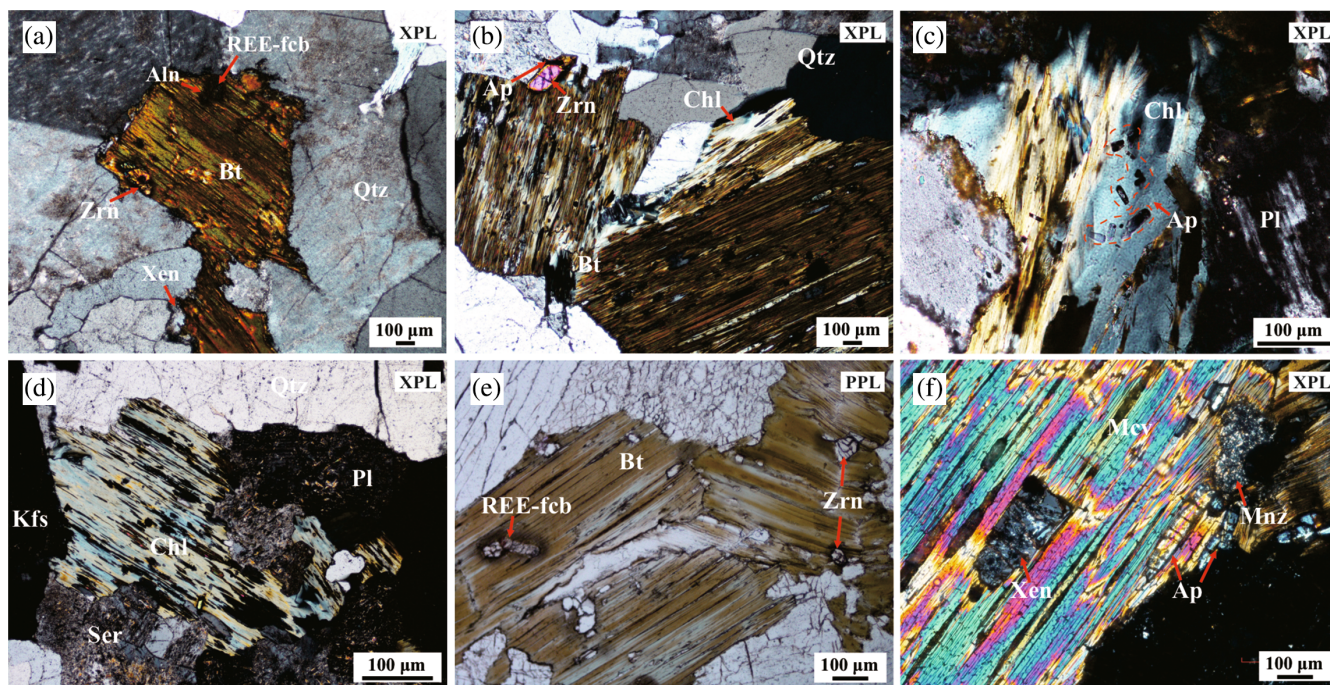


FIGURE 6 Photomicrographs of sample TBKP-38 PG: (a) REE-fluorocarbonate and zircon inclusions in biotite, (b) Apatite within zircon inclusion in biotite, which is partly altered into chlorite, (c) Apatite inclusion in chloritized biotite, (d) Chloritized biotite and sericitized feldspar, (e) REE-fluorocarbonate and zircon inclusions with metamict halo in biotite altered to muscovite, (f) Xenotime, apatite, and monazite in muscovite after biotite. Aln, allanite; Ap, apatite; Bt, biotite; Chl, chlorite; Kfs, k-feldspar; Mcv, muscovite; REE-fcb, REE-fluorocarbonate; Qtz, quartz; Xen, xenotime; Zrn, zircon.

by volume (Figure 4). The secondary minerals observed in this granite are 2% chlorite and 11% sericite. Similarly, sample TBKP-38 is classified as granite based on the modal abundance of quartz, alkali feldspar, and plagioclase following the IUGS classification. The modal composition for this sample includes 56% orthoclase, 6% plagioclase, 22% quartz, 3% biotite, and 2% muscovite. Accessory minerals such as zircon, apatite, and ilmenite are present in amounts less than 1% by volume. The secondary minerals in this parent granite include chlorite (Figure 6), which is below 1%, and 8% sericite.

In general, REE-bearing minerals that are present both in TBKP-30 and TBKP-38 granite tend to occur as inclusion in biotite. Three groups of REE-bearing minerals were found in the parent granite samples: fluorocarbonate, silicate, and phosphate minerals. The SEM-EDS analysis confirmed that these minerals are enriched in cerium except xenotime, including monazite-(Ce) ($\text{Ce, La, Nd, Th})\text{PO}_4$ (Figure 7d), xenotime (YPO_4), allanite-(Ce) ($\text{Ce, Ca, Y})_2(\text{Al, Fe}^{3+})_3(\text{SiO}_4)_3(\text{OH})$ (Figure 7b), and parisite-(Ce) $\text{Ca}(\text{Ce, La})_2(\text{CO}_3)_3\text{F}_2$ (Figure 7e–i). These are supported by the corresponding SEM-EDS spectra and mineral chemistry. REE-fluorocarbonates are identified in cracks of altered K-feldspar (Figure 7e), cavities of quartz as anhedral shape (Figure 7g), and filling the biotite cleavage (Figure 9f).

REE-bearing minerals identified within this granite (TBKP-30) include REE-fluorocarbonates such as synchysite and parisite. Florencite is recognized in weathering environment (Figure 8d,e). Thus, while biotite is the dominant host for REEs in this granite, K-feldspar also contributes to the REE inventory (Figure 7e), particularly for specific REE-fluorocarbonates.

Primary REE-bearing minerals are less abundant in the weathered sample compared to the parent granite. This sample only contains a few REE minerals such as monazite, xenotime, florencite (Figure 8a–c), and zircon as resistant minerals (Figure 8f). In weathered samples obtained from parent granite, there is a noticeable reduction in the occurrence of minerals containing rare earth REEs compared to the unaltered parent granite. However, monazite recognized within the weathered sample stands out as a rare occurrence (Figure 8c). This observation suggests that monazite was selectively retained or preserved during the weathering process.

In the parent granite TBKP-38, REE-fluorocarbonates are also recognized within biotite, associated with minerals like allanite, apatite and zircon (Figure 9a–c). Instead, REE-bearing phases are found as secondary minerals, particularly cerianite and residual monazite (Figure 10d) and xenotime (Figure 10e), associated with Mn-Fe oxides and kaolinite in the weathered samples. In

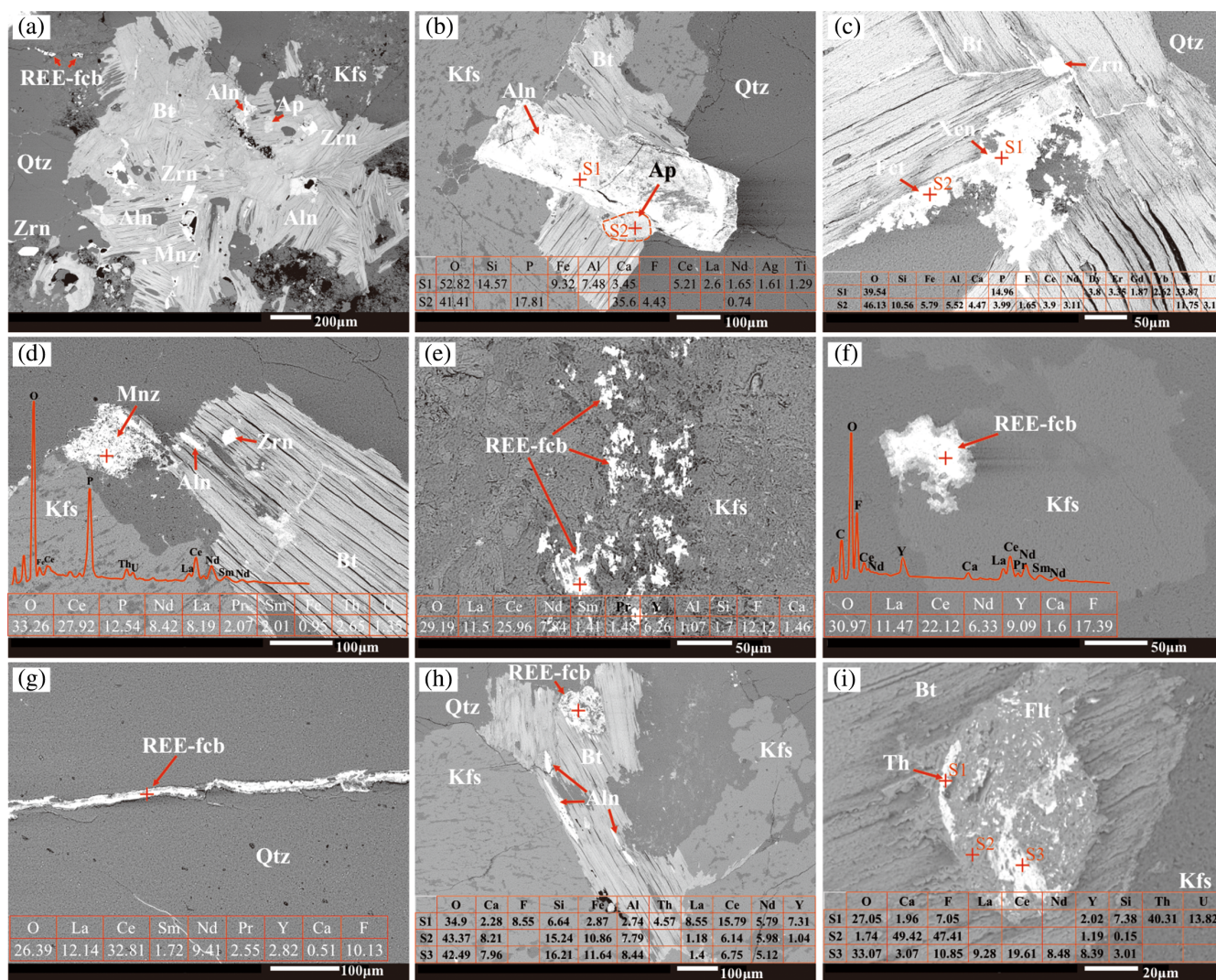


FIGURE 7 Backscattered Electron (BSE) images of REE-bearing mineral; allanite, apatite, monazite, xenotime, zircon, and REE-fluorocarbonate (synchysite, parisite) in TBKP-30 parent granite: (a) Wide-view of REE-bearing minerals within biotite. (b) Allanite-(Ce) and fluoroapatite. (c) Zircon and irregular shape florencite-(Ce) associated with xenotime. (d) Monazite-(Ce) hosted in biotite. (e, f) Acicular synchysite-(Ce) within cracks K-feldspar and (g) Within quartz, (h) Replacing precursor allanite, and (i) Thorite, and REE-fluorocarbonate occur within fluorite in biotite. Aln, allanite; Ap, apatite; Bt, biotite; Chl, chlorite; Flt, fluorite; Kfs, k-feldspar; Mcv, muscovite; Mnz, monazite; REE-fcb, REE-fluorocarbonate; Th, thorite; Qtz, quartz; Xen, xenotime; Zrn, zircon.

Figure 10a,b, cerianite occurs as fine-grained aggregates and is attached to the surfaces of Mn-Fe oxides and within kaolinite (Figure 10c). Monazite is found incorporated with Fe-oxides on the grain boundaries of quartz (Figure 10f).

4.2 | XRD characterization in weathered granite

The XRD data from TBKP-30 indicate that the bulk mineral composition is mostly quartz and kaolinite (Figure 3). Gibbsite occurs in the upper and lower zones. B5 and B7 show a higher abundance of gibbsite

compared to the other samples, with kaolinite being the most abundant clay mineral.

The weathered samples were thoroughly analyzed for their clay content. The results indicate the presence of kaolinite and gibbsite in both the lower and upper parts of the TBKP-30 profile (Figure 3a). In TBKP-30, gibbsite occurs randomly in the weathered samples with kaolinite, but the gibbsite peaks increase when the kaolinite peaks decrease. This suggests gibbsite form from kaolinite in intensely weathered samples. In TBKP-38, gibbsite only occurs mainly in the top soil layer (A) with small peaks in B1 and B3 (Figure 3b). In this core, there is a minor peak of illite in B4 and C. In the lower part of B4 and C, a K-feldspar peak is still present.

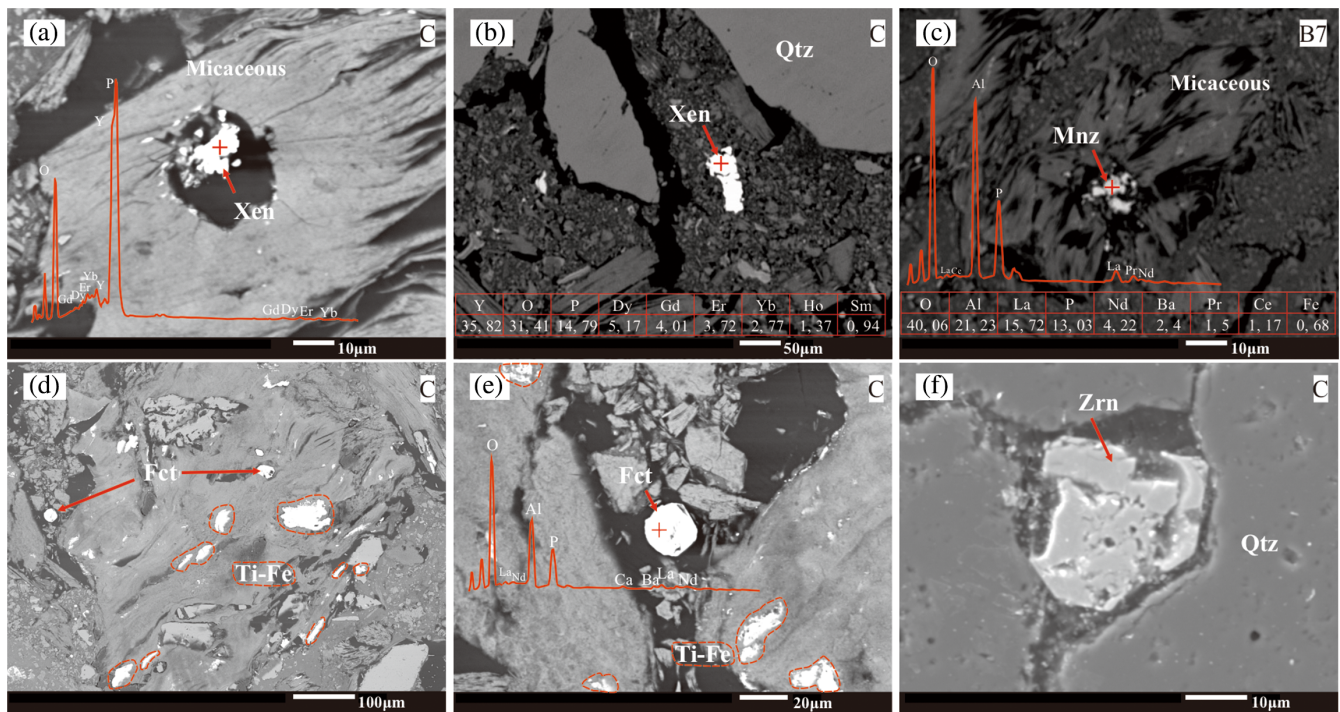


FIGURE 8 BSE images from weathered sample c zone of TBKP-30 samples. (a) Xenotime grain in micaceous particle and (b) Xenotime remains in kaolinized feldspar. (c) Monazite in weathered biotite. (d–e) Forencite form in weathered mica. (f) Weathered zircon within quartz. Fct, florencite; Mnz, monazite; Qtz, quartz; Xen, xenotime; Zrn, zircon.

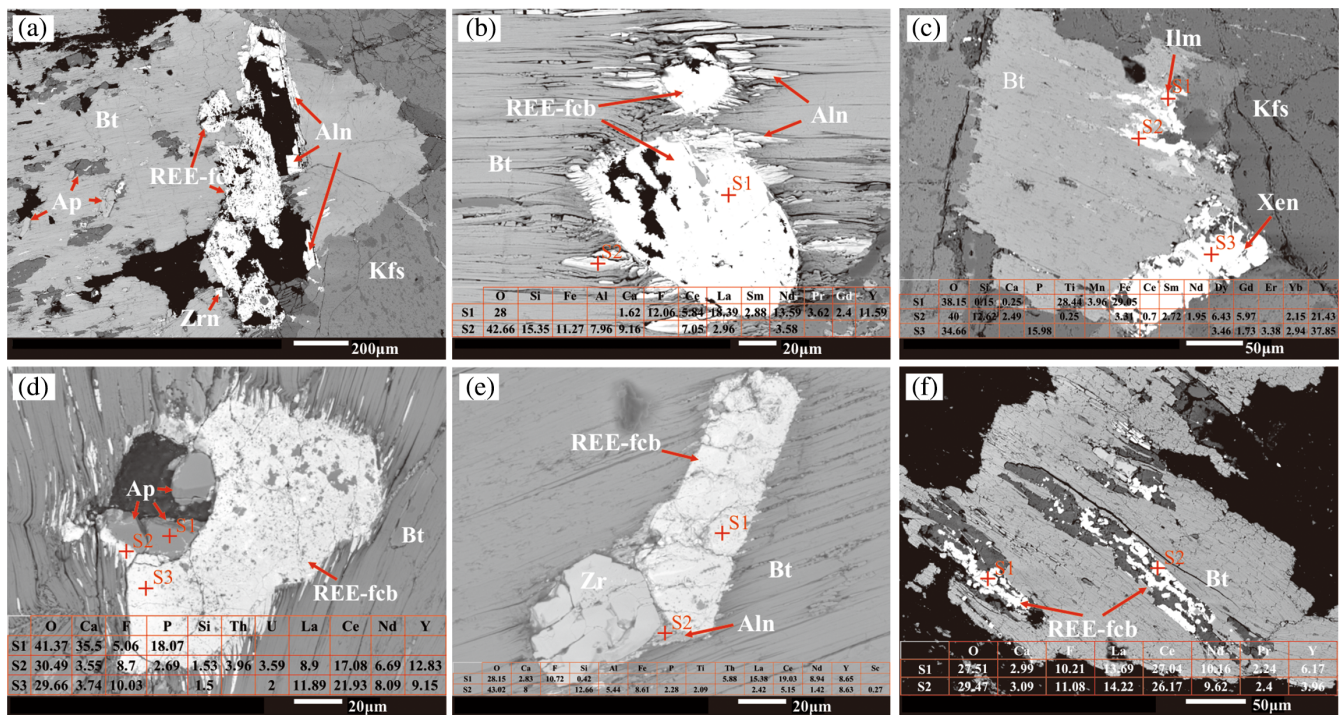


FIGURE 9 BSE image of TBKP-38. (a–c) REE-bearing minerals hosted in biotite in parent granite samples; allanite, apatite, REE-fluorocarbonate, xenotime, and zircon. (d) REE-fluorocarbonate half replaced apatite, (e) Precursor allanite within biotite, and (f) Filling biotite cracks. Aln, allanite; Ap, apatite; Bt, biotite; Kfs, k-feldspar; REE-fcb, REE-fluorocarbonate; Qtz, quartz; Xen, xenotime; Zrn, zircon.

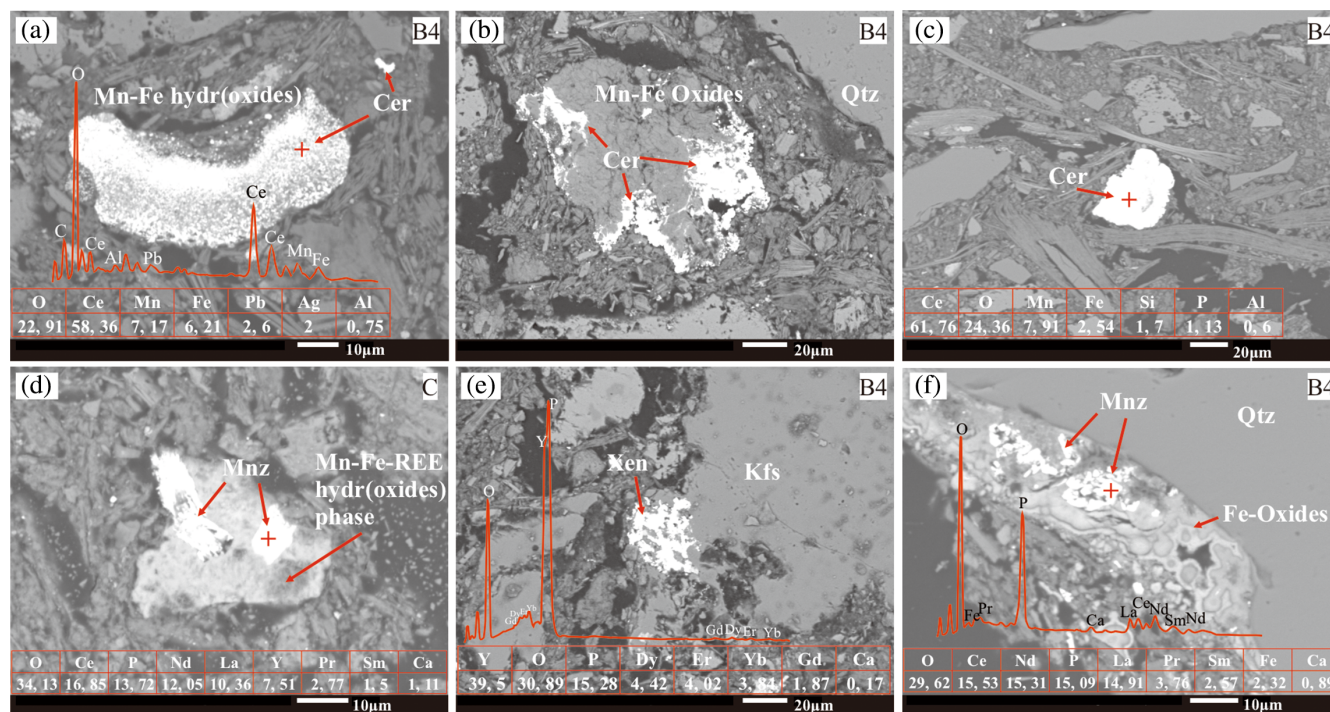


FIGURE 10 BSE image from weathered zone of TBKP-38 samples. (a, b) Secondary cerianite occurs as fine-grained aggregate on the surface of Mn-Fe oxide. (c) Cerianite in kaolinite. (d) Monazite as a residual mineral in Fe-Mn (hydr)oxides, (e) Xenotime within K-feldspar. (f) Monazite within Fe-oxides on grain boundary of quartz. Cer, cerianite; Mnz, monazite; Kfs, K-feldspar; Qtz, quartz; Xen, xenotime.

4.2.1 | Geochemistry of granite and weathered granite

Topsoil sample (30-A) at a depth of 0.5 m shows a SiO₂ content of 82.69 wt.%, Al₂O₃ content is 9.36 wt.%, while Fe₂O₃(T) is 1.55 wt.%, indicating modest aluminum and iron oxides concentrations. Limonite to saprolite zone samples (30-B1 to 30-B7) SiO₂ content ranges from 65.53 to 72.78 wt.%, showing silica abundance fluctuation. Al₂O₃ content varies from 15.01 to 21.26 wt.%, reflecting changes in aluminum oxide concentrations. Fe₂O₃(T) content ranges from 2.49 to 6.7 wt.%. Similarly, other elements such as MnO, MgO, CaO, Na₂O, K₂O, TiO₂, P₂O₅, Loss on Ignition (LOI), and total composition exhibit discernible variations across the sampled depths (Figure 11). 30-C also has a high silica content. Al₂O₃ content is 10.79 wt.%, and Fe₂O₃(T) is 1.71 wt.%, suggesting a distinct geochemical profile compared to other zones. Finally, the parent granite rock sample (30-PG) at a depth of 18 m shows a SiO₂ content of 73.97 wt.%.

REEs content for profiles TBKP-30 and TBKP-38 show variability within the depth (Table 1). Profile TBKP-30, with samples collected from depths of 0.5 m to 18 m shows LREE concentrations ranging from 13.73 to 76.62 ppm and HREE values between 12.44 and 45.38 ppm. The total REE plus Y (REEY) content spans from 29.94 to 1279.53 ppm, with LREE/HREE ratios

varying from 1.07 to 2.84 and La/Yb ratios from 0.70 to 4.41. REE content in this profile peak at 30-B7 (17m).

In profile TBKP-38, LREE concentrations range from 10.64 to 1002.2 ppm while HREE values are between 21.44 and 204 ppm with sample depths from 1 m to 15 m. The total REEY from 69.77 to 1315.0 ppm. The LREE/HREE ratios in this profile vary from 0.59 to 4.11, and La/Yb ratios range from 0.46 to 15.63. Ce enrichment is observed at sample 38-B4 (12m), while other REEs do not show significant enrichment. Sample 38-PG shows the highest La/Yb ratio, indicating LREE enrichment. Both profiles contain high abundance of LREEs compared to HREEs, with the LREE/HREE and La/Yb ratios indicating significant LREE enrichment in certain samples.

5 | DISCUSSION

5.1 | REE-bearing minerals in parent granite

Both granites show that they are enriched in REE. LREE/HREE ratios for TBKP-30 and TBKP-38 were 9.16 and 2.35, respectively. The REE content is primarily derived from REE-bearing silicates (allanite), phosphates (monazite, xenotime), and secondary fluorocarbonates (parisite, synchysite). Although thorite (Figure 7i), zircon

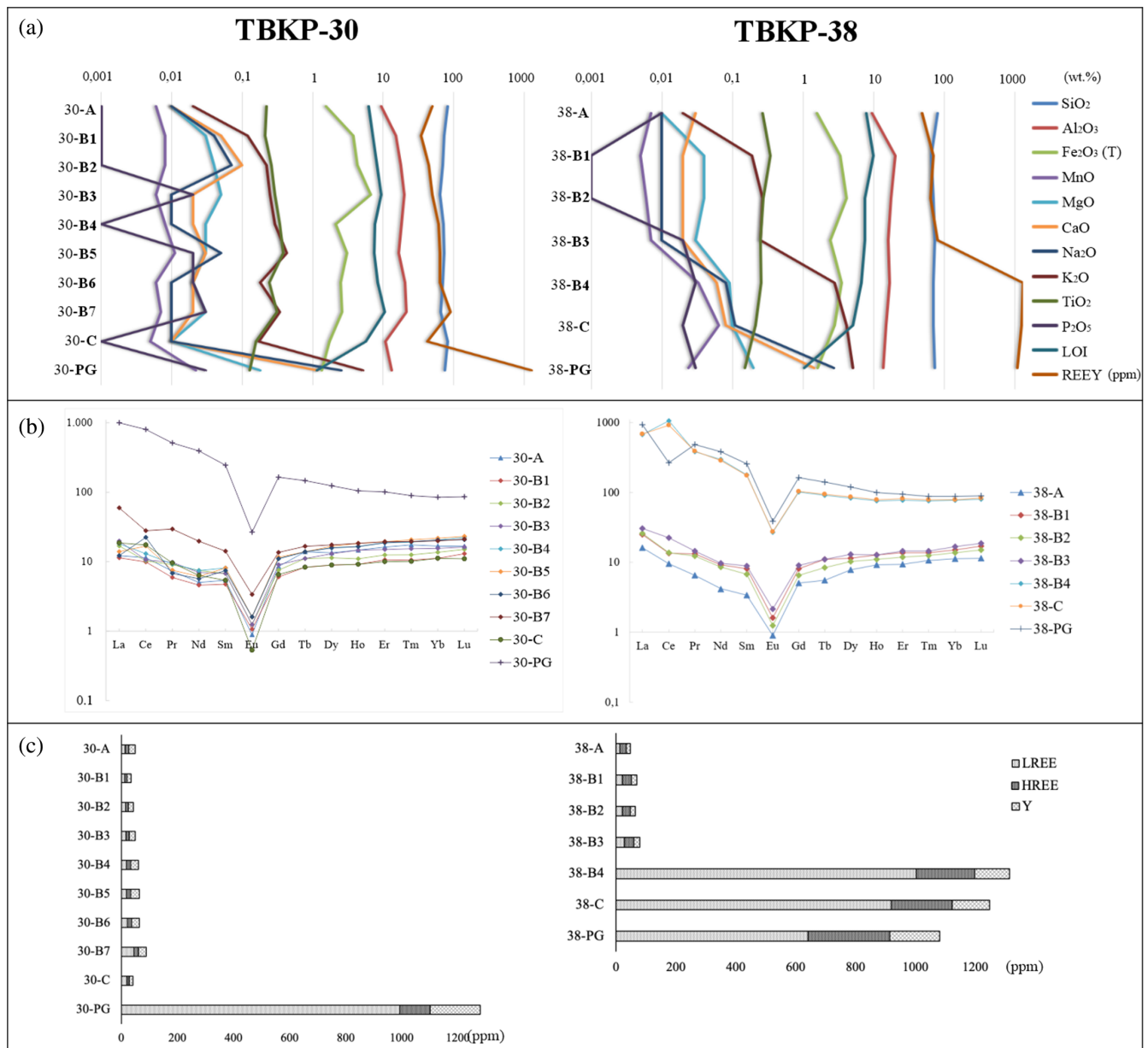


FIGURE 11 (a) Distribution content of major oxides, LOI and REEY (ppm), (b) REE enrichment pattern (ppm) along both profiles, and (c) Chondrite normalized REE pattern (McDonough & Sun, 1995).

(Figure 7c), and apatite are present, they are not significant sources of REEs. Fluorapatite (Figure 9d) was partially altered into REE-fluorocarbonates.

Xing et al. (2023) suggest that REEs in fluorapatite can remobilize and precipitated into REE fluorocarbonates through hydrothermal alteration. Fluorite is also observed in the parent granite as a secondary mineral (Figure 7i). This suggests that fluorite precipitation occurred by an involvement of hydrothermal solutions. It may have also been caused by fluid mixing or interactions with the wall rock (Sharma & Srivastava, 2014; Wang et al., 2020). The presence of fluorite further

supports the role of hydrothermal fluids in the alteration of the granite.

REE-fluorocarbonates (parisite, synchysite) are present in the parent granite. They occur in altered K-feldspar, within perthite cracks, quartz cavities as anhedral crystals, and filling the cleavage of biotite. Chlorite (Figure 6c,d) and muscovite (Figure 6f), products of biotite alteration, are also observed. These minerals are formed through hydrothermal processes, where REE-rich aqueous solutions permeate the granite, leading to the crystallization of REE-bearing phases during the intermediate magmatic-hydrothermal to late hydrothermal stages

TABLE 1 Chemical composition of the weathered granite and parent granite in South Bangka.

Profile Sample	TBKP-30										TBKP-38									
	30-A	30-B1	30-B2	30-B3	30-B4	30-B5	30-B6	30-B7	30-C	30-PG	38-A	38-B1	38-B2	38-B3	38-B4	38-C	38-PG			
Depth (m)	0.5	1.4	2.2	5	8.3	9.2	11.5	13.8	17	18	1.5	3	5.3	8.8	13	15	15.2			
SiO ₂ (wt.%)	82.69	72.21	69.81	62.96	70.69	72.78	69.28	65.53	81.24	73.97	81.27	64.85	70.06	73.46	70.17	70.86	74.18			
Al ₂ O ₃	9.36	15.01	17.85	19.83	18.28	16.64	20.28	21.26	10.79	13.09	9.5	20.47	17.53	16.22	17	15.14	13.62			
Fe ₂ O ₃ (T)	1.55	3.77	4.29	6.7	2.11	3.02	2.49	2.61	1.71	1.34	1.58	3.37	4.12	2.46	3.52	2.77	1.61			
MnO	0.006	0.008	0.008	0.006	0.008	0.011	0.006	0.007	0.005	0.022	0.007	0.005	0.006	0.007	0.033	0.064	0.024			
MgO	0.01	0.03	0.04	0.05	0.03	0.03	0.02	0.03	0.01	0.18	0.01	0.04	0.04	0.03	0.09	0.1	0.2			
CaO	0.01	0.05	0.1	0.02	0.02	0.03	0.02	0.02	0.01	1.18	0.03	0.02	0.02	0.02	0.06	0.08	1.45			
Na ₂ O	0.01	0.04	0.07	0.01	0.01	0.05	0.01	0.01	0.01	2.55	0.01	0.01	0.01	0.01	0.08	0.11	2.75			
K ₂ O	0.02	0.12	0.22	0.25	0.29	0.43	0.18	0.34	0.17	5.17	0.02	0.19	0.27	0.25	2.78	4.1	5.04			
TiO ₂	0.223	0.209	0.258	0.29	0.344	0.38	0.244	0.309	0.158	0.129	0.269	0.342	0.273	0.247	0.258	0.212	0.152			
P ₂ O ₅	<0.01	<0.01	<0.01	0.02	<0.01	0.02	0.02	0.03	<0.01	0.03	0.01	<0.01	<0.01	0.02	0.03	0.02	0.03			
LOI	6.22	7.15	8.09	9.44	7.55	7.44	8.35	10.38	5.64	1.14	7.95	9.89	7.61	7.58	6.74	5.1	1.03			
Total (%)	100.1	98.61	100.7	99.57	99.33	100.8	100.9	100.5	99.76	98.8	100.7	99.18	99.94	100.3	100.8	98.56	100.1			
CIA (%)	99.57	98.62	97.86	98.61	98.28	97.03	98.98	98.29	98.27	59.53	99.37	98.94	98.32	98.30	85.34	77.92	59.58			
Be (ppm)	<1	<1	<1	1	1	<1	1	<1	<1	5	<1	<1	<1	1	3	3	4			
V	14	22	25	34	13	19	14	17	10	8	16	28	22	13	18	14	10			
Cr	<20	<20	<20	<20	<20	<20	<20	<20	<20	40	<20	<20	<20	<20	<20	<20	50			
Co	<1	1	1	1	1	1	1	1	1	2	1	1	1	1	2	7	2			
Ni	<20	<20	<20	<20	<20	<20	<20	<20	<20	20	<20	<20	<20	<20	<20	<20	20			
Cu	10	60	20	50	<10	<10	<10	10	<10	<10	<10	<10	<10	<10	<10	<10	<10			
Zn	<30	60	30	50	30	30	30	<30	<30	<30	<30	<30	<30	<30	30	30	<30			
Ga	15	20	25	31	26	23	24	26	14	17	15	29	25	22	25	22	19			
Ge	1	1	1	2	2	1	2	1	<1	1	1	2	2	2	2	2	1			
As	9	14	17	22	<5	<5	<5	<5	<5	<5	9	17	18	19	17	14	9			
Rb	4	15	27	37	45	63	31	58	25	304	3	29	41	47	332	324	314			
Sr	2	3	3	<2	<2	<2	<2	<2	<2	116	3	<2	<2	<2	16	22	86			
Zr	239	125	175	180	220	275	186	231	145	103	312	222	200	178	223	153	139			
Nb	10	10	14	19	20	23	16	23	8	6	11	21	16	18	19	14	10			
Mo	2	3	3	4	<2	3	2	2	2	<2	3	3	3	2	2	<2	2			
Ag	<0.5	<0.5	<0.5	<0.5	<0.5	<0.5	<0.5	<0.5	<0.5	<0.5	<0.5	<0.5	<0.5	<0.5	<0.5	<0.5	<0.5			

TABLE 1 (Continued)

Profile Sample	TBKP-30										TBKP-38									
	30-A	30-B1	30-B2	30-B3	30-B4	30-B5	30-B6	30-B7	30-C	30-PG	38-A	38-B1	38-B2	38-B3	38-B4	38-C	38-PG			
In	<0.2	0.2	0.2	0.2	<0.2	<0.2	<0.2	<0.2	<0.2	<0.2	<0.2	<0.2	<0.2	<0.2	<0.2	<0.2	<0.2			
Sn	60	16	11	19	5	4	3	672	3	1	54	18	4	3	3	3	2			
Sb	<0.5	<0.5	0.5	1	<0.5	0.5	<0.5	<0.5	<0.5	<0.5	<0.5	0.5	0.6	<0.5	<0.5	<0.5	<0.5			
Cs	0.6	1	1.4	1.6	1.7	2.1	1.2	1.6	1.1	7.4	<0.5	1.4	1.5	1.6	21.6	11.5	6.7			
Ba	6	6	8	10	8	11	5	10	6	847	5	8	8	12	115	199	106			
Bi	0.8	0.9	2.6	1.9	0.4	<0.4	<0.4	<0.4	<0.4	<0.4	0.6	0.6	<0.4	<0.4	<0.4	<0.4	<0.4			
La	2.9	2.7	4	4.7	4.3	3.3	2.9	14.1	4.4	237	3.8	5.9	6.1	7.2	159	162	222			
Ce	7	6.1	6.3	6.5	8	10.3	13.7	17.1	10.7	491	5.8	8.3	8.4	13.6	645	563	162			
Pr	0.68	0.55	0.84	0.91	0.86	0.7	0.63	2.74	0.89	47.4	0.6	1.22	1.13	1.33	35.5	35.8	44.9			
Nd	2.3	2.1	3.4	3.2	3.4	2.8	2.6	9	2.9	180	1.9	4.2	3.9	4.4	135	131	173			
Sm	0.8	0.7	1	1	1.2	1.2	1.1	2.1	0.8	36.2	0.5	1.2	1	1.3	26.2	25.8	37.5			
Eu	0.05	0.06	0.07	0.07	0.09	0.09	0.09	0.19	0.03	1.5	0.05	0.09	0.07	0.12	1.5	1.54	2.19			
Gd	1.7	1.2	1.5	1.8	2.2	2.3	2.2	2.7	1.3	32.8	1	1.6	1.3	1.8	20.3	20.5	32.3			
Tb	0.5	0.3	0.4	0.4	0.5	0.5	0.5	0.6	0.3	5.3	0.2	0.4	0.3	0.4	3.3	3.4	5.1			
Dy	3.3	2.2	2.8	3.2	3.9	4.1	3.9	4.3	2.2	30.5	1.9	2.8	2.5	3.2	20.5	21	29.1			
Ho	0.8	0.5	0.6	0.8	0.9	1	0.9	1	0.5	5.7	0.5	0.7	0.6	0.7	4.1	4.3	5.4			
Er	2.6	1.7	2	2.4	3	3.1	3	3.1	1.6	16.2	1.5	2.2	1.9	2.3	12.4	13.1	15			
Tm	0.43	0.26	0.31	0.38	0.47	0.51	0.48	0.48	0.25	2.21	0.26	0.34	0.31	0.36	1.87	1.95	2.15			
Yb	2.7	1.8	2.2	2.5	3.3	3.5	3.3	3.2	1.8	13.6	1.8	2.4	2.2	2.7	12.4	12.7	14.2			
Lu	0.41	0.32	0.37	0.4	0.55	0.57	0.51	0.52	0.27	2.12	0.28	0.42	0.37	0.46	1.98	2.05	2.2			
Hf	7.3	4	5.7	6.1	7.6	8.6	5.9	7.7	4.5	3.3	9.3	7.5	6.6	6	7.3	4.9	4.4			
Ta	1.6	1.7	2.3	2.7	4.5	3.4	2.3	3.1	1.3	1.2	1.5	2.7	2.5	2.6	2.6	2	1.4			
W	3	5	3	4	11	2	2	2	<1	2	3	3	4	2	2	1	4			
Tl	0.2	<0.1	0.2	0.2	0.2	0.3	0.1	0.2	0.2	1.2	0.3	0.1	0.2	0.2	1.8	1.7	1.4			
Pb	5	6	8	10	10	8	10	43	11	26	5	11	9	43	58	50	27			
Th	36.3	79.4	94.6	155	61.5	74.7	67.3	85.1	44	38.3	32.7	84.9	102	82.8	97.9	72.6	50.7			
U	3.6	2.8	3.3	4.1	5.9	10.3	5.8	27.7	10.4	9.3	3.6	4	4.1	6.3	19.4	13.1	9.5			
LREE	13.73	12.21	15.61	16.38	17.85	18.39	21.02	45.23	19.72	993.1	12.65	20.91	20.6	27.95	1002.2	919.14	641.59			
HREE	12.44	8.28	10.18	11.88	14.82	15.58	14.79	15.9	8.22	108.43	21.44	29.86	26.48	31.92	194.85	204	272.45			
Sc (ppm)	2	3	4	5	4	5	4	5	3	3	2	5	4	5	9	6	4			

(Continues)

TABLE 1 (Continued)

Profile Sample	TBKP-30										TBKP-38									
	30-A	30-B1	30-B2	30-B3	30-B4	30-B5	30-B6	30-B7	30-C	30-PG	38-A	38-B1	38-B2	38-B3	38-B4	38-C	38-PG			
Y	23	14	18	21	28	28	28	28	14	178	14	19	17	20	118	125	167			
REE + Y	49.17	34.49	43.79	49.26	60.67	63.97	63.81	89.13	41.94	1279.53	48.09	69.77	64.08	79.87	1315.05	1248.14	1081.04			
LREE/HREE	1.10	1.47	1.53	1.38	1.20	1.42	2.84	2.40	2.40	9.16	0.59	0.70	0.78	0.88	5.14	4.51	2.35			
La/Yb	1.07	1.50	1.82	1.88	1.30	0.94	0.88	4.41	2.44	17.43	2.11	2.46	2.77	2.67	12.82	12.76	15.63			

Note: Fe_2O_3 total ion oxides, CIA chemical index of alteration = $[(\text{Al}_2\text{O}_3/\text{Al}_2\text{O}_3 + \text{CaO} + \text{Na}_2\text{O} + \text{K}_2\text{O})] \times 100$, (Nesbitt, 1979).

(Louvel et al., 2022; Schmandt et al., 2017; Tampubolon et al., 2022; Xing et al., 2023).

5.2 | Distribution of REEs in the weathering profile

The REE-fluorocarbonates are the main source of the enrichment in this weathered profile due to their easily dissolving during the weathering process. Cerium, the most enriched element in the weathered profile, was associated with Mn-Fe Oxides and inherited the REE signature that reflects high cerium from the parent granite (Table 2). This is possibly due to simultaneous oxidative precipitation (Santos et al., 2019; Xu et al., 2017).

Sample C horizon in TBKP-38 shows a positive cerium anomaly. The high concentration of cerium in the TBKP-38 weathered profile can be attributed to the presence of cerianite and monazite-(Ce) in the saprock and saprolite zone as shown in Figure 10c,d. The existence of xenotime within weathered biotite (Figure 8a) and residual and authigenic monazite and xenotime (Figure 8b,c) suggests that certain rare earth elements repositioned next to the REE-bearing original minerals. In contrast, others were created during the initial weathering process in the presence of oxidizing conditions (Radusinovi et al., 2017). There is a possibility that REEs in this study were mostly not absorbed onto the surface of clays such as kaolinite (Sanematsu et al., 2013, 2015).

Geochemical analysis of TBKP-30 indicates that the weathering profile of this sample does not exhibit any enrichment of REE. The high abundance of gibbsite over kaolinite is evident from the results of the XRD analysis as shown in Figure 3. This indicates that strong weathering formed gibbsite from kaolinite. Due to dissolution of kaolinite, REEs were leached out from the weathering profile completely, resulting in the poor concentration of REEs in this drill hole. The small amounts of REEs remaining are due to the presence of refractory REE-bearing minerals in the drilled samples.

Figure 3 shows that the CIA values in both profiles have different values. Compared to the REE enrichment graph in both profiles in Figure 11c, it displays that REE only occurs in horizon C of TBKP-38. This indicates that the REE in TBKP-30 is highly weathered, resulting in the occurrence of gibbsite, which may cause the REE ions not to attach to secondary minerals (Sanematsu et al., 2009, 2013; Zhao et al., 2024). The lack of REE enrichment in TBKP-30 could potentially be ascribed to the conditions prevailing near a fault line, where groundwater movement might facilitate the migration of REE ions to adjacent areas. Furthermore, the occurrence of gibbsite, indicative of advanced surface weathering,

TABLE 2 EPMA analysis from representative REE-bearing minerals in parent granite.

Sample no	Apatite	Allanite	Xenotime	Fluorocarbonate
<i>n</i>	11	20	6	16
F (wt.%)	6.47	0.05	0.44	8.08
Al ₂ O ₃	0.00	15.51	0.00	0.32
P ₂ O ₅	41.57	0.01	32.81	0.30
K ₂ O	0.00	0.01	0.01	0.02
CaO	53.62	10.29	0.04	4.54
La ₂ O ₃	0.03	1.61	0.00	10.74
Ce ₂ O ₃	0.18	7.16	0.03	23.22
Nd ₂ O ₃	0.18	7.26	0.04	9.11
Pr ₂ O ₃	0.02	1.17	0.01	2.35
Sm ₂ O ₃	0.06	2.31	0.13	1.87
Dy ₂ O ₃	0.13	0.56	5.43	1.08
Gd ₂ O ₃	0.09	1.20	3.26	1.54
UO ₂	0.00	0.00	0.00	0.09
SiO ₂	0.54	31.16	0.37	1.83
Y ₂ O ₃	0.73	0.72	43.34	5.49
TiO ₂	0.02	0.26	0.01	0.00
Cl	0.01	0.03	0.00	0.04
FeO	0.24	15.97	0.17	0.82
ThO ₂	0.01	0.31	0.16	5.26
Er ₂ O ₃	0.04	0.02	3.15	0.18
TREEO	1.46	21.99	55.39	55.58
Total	101.21	95.56	89.22	73.48

Note: *n*, no. microprobe points.

reinforces this interpretation. In TBKP-30, three distinct gibbsite layers are present, while TBKP-38 exhibits two such layers (Figure 3), suggesting that the groundwater level likely experienced abrupt fluctuations two or three times, which may have further influenced REE redistribution within these weathering profiles (Huang, He, et al., 2021a).

5.3 | Possibility for ion adsorption-type REE mineralization

During weathering, the stability and composition of primary REE-bearing minerals strongly affect REE fractionation and secondary mineral formation (Fu et al., 2019; Huang, Tan, et al., 2021b; Mukai et al., 2020; Nesbitt, 1979; Sanematsu et al., 2013, 2015; Santana et al., 2015; Yusoff et al., 2013). In this study, parent granite was mainly composed of feldspar, quartz, biotite and lack of amphibole (Figures 5 and 6), while the dominant REE-bearing minerals were REE-fluorocarbonates, and REE phosphates, along with apatite, allanite, and zircon.

Although zircon occurs as an REE-bearing mineral in the weathered profile, it remains resistant to alteration (Figure 8f). REE-fluorocarbonates commonly occur in cavities or along cracks and grain boundaries of feldspars in the parent granite (Figure 7) and they also infill the biotite cracks. Rock-forming minerals decompose along with REE-bearing minerals, leading to the formation of clay minerals and Fe-Mn (hydr)oxides. The K₂O, Na₂O, MgO, and CaO contents decreased, indicating mineral breakdown. While the REEs are released and concentrated in the soil profile, they can be adsorbed onto clay minerals and incorporated in primary or secondary minerals (Sanematsu & Watanabe, 2016).

In the regolith profile, it is possible that leached REEs were relatively incorporated onto Fe-Mn hydr(oxides) and cerianite in the lower profile, as suggested by the presence of Fe-Mn hydr(oxides) (Figure 10a,b,d) and positive Ce anomalies (Figure 11b) in this samples. Positive Ce anomaly commonly occurs in the upper profile of regolith as REE-leached zone due to the simultaneous oxidative precipitation and low to medium pH. In these conditions, cerianite forms due to pH control over Ce⁴⁺

fixation (Abedini et al., 2020; Sanematsu et al., 2013; Sanematsu & Watanabe, 2016; Santos et al., 2019). Anatase Ti-bearing minerals were also present in the C zone as shown in Figure 8d, which also indicates a reducing and low pH (Radusinovi et al., 2017).

Ion adsorption-type REE deposits are thought to originate from extensive weathering in tropical regions, where primary rock-forming minerals and REE-bearing minerals break down quickly due to high precipitation rates that dissolve minerals and release REE ions (Sanematsu & Watanabe, 2016; Schoonheydt & Johnston, 2013). Significant REE leaching happens in the uppermost layer of laterite during weathering, while REEs tend to gather as secondary minerals in the lower portion of the regolith (Berger et al., 2014; Chapela Lara et al., 2018) or they may occur via adsorption onto clay minerals (Li & Zhou, 2020; Yusoff et al., 2013) and iron-manganese (hydr)oxides (Braun et al., 2018; Duzgoren-Aydin & Aydin, 2009).

In the study area, the weathering products mainly consist of quartz, kaolinite, and gibbsite determined by XRD analysis. Secondary minerals such as kaolinite and gibbsite result from the decomposition of feldspar minerals weathering that occurred in warm, humid paleoclimatic conditions (Mellor & Wilson, 1989; Wilke & Schwertmann, 1977). Kaolinite is not a product of ancient weathering but is only found in modern soil that overlies deep weathered material (Torrent & Benayas, 1977). Minerals such as the kaolinite group mineral, occurred in the lower part of the weathering profile in a more alkaline environment closer to the water table (Borst et al., 2020; Giovannini et al., 2021).

A preliminary analysis of the discussion indicates that the REE enrichment observed from horizon C to B in the TBKP-38 profile appears to be driven primarily by cerium enrichment rather than by an ion adsorption mechanism involving kaolinite and illite (Figure 3). However, their presence may also facilitate the ion adsorption mechanism. Other REEs, besides cerium, are depleted compared to the parent granite. This is likely a result of the oxidation and fixation of Ce as CeO_2 or its incorporation with Fe-Mn (hydr)oxides and the relatively lower degree of weathering (CIA < 85%) in these samples compared to more weathered ones (TBKP-30). The remainder of the profile has undergone such intense weathering that gibbsite has formed from kaolinite, rendering it unsuitable for ion-adsorption mineralization. For future exploration, it is suggested that weathering profiles devoid of gibbsite be targeted.

6 | CONCLUSION

The Klabat granite, exhibiting characteristics of S-type granite, serves as the precursor rock for regolith-hosted REE mineralization. REE-fluorocarbonates, predominantly found

within cavities, along grain boundaries, and within cracks in feldspars, emerges as the primary REE source for mineralization due to its susceptibility to dissolution in acidic soil water. REE ions that removed from the solution are mainly incorporated into secondary minerals as Mn-Fe (hydr)oxides. REE phosphates are more resistant in the weathering profile. The parent granite, possessing REEY concentrations ranging from 1081 to 1279 ppm, demonstrates enrichment in light rare earth elements (LREE) relative to heavy rare earth elements (HREE), with ratios of 2.35–9.16.

The weathering profile atop the parent granite is delineated into upper and lower segments by a redox boundary near a depth of approximately 8.5 m. The upper segment represents a leached zone devoid of a positive Ce anomaly and exhibits significantly lower REE contents. In contrast, the lower segment manifests as an accumulation zone characterized by a positive Ce anomaly, with slightly augmented REE contents enriched from parent granite 1081 to 1315 ppm in the weathered profile (as observed in the TBKP-38 profile). These findings suggest that the depletion and enrichment of REEs arise from the migration of REEs from the upper to the lower segment of the profile. The positive Ce anomaly in the lower segment suggests the fixation of Ce^{4+} under oxidizing and acidic conditions.

ACKNOWLEDGMENTS

We would like to express our thanks for the REE inventory project funded by the Centre for Mineral Coal and Geothermal Resources. Special thanks to Dr. Takuya Echigo for his helpful comments and to Dr. Carmela Alen Tupaz for her assistance with the laboratory work and feedback. We also thank the Mineral Resource Tectonic Group (Akita University) for the financial support in analyzing the samples. We would like also to extend our gratitude to Dr. Tatsuo Nozaki, Associate Editor of *Resource Geology*, as well as to Dr. Arifudin Idrus and the anonymous reviewer for their thoughtful and insightful comments, which have greatly contributed to the improvement of this manuscript.

CONFLICT OF INTEREST STATEMENT

Dr. Yasushi Watanabe is the Editor-in-Chief of the journal and the co-author of this article. They were excluded from the peer-review process and all editorial decisions related to the acceptance and publication of this article. Peer-review was handled independently by RGE Journal editorial office and Dr. Tatsuo Nozaki as the Editor to minimize bias.

DATA AVAILABILITY STATEMENT

The data that support the findings of this study are available from the corresponding author upon reasonable request.

ORCID

Yusuf Zaki Agung  <https://orcid.org/0000-0001-6871-3814>

Yasushi Watanabe  <https://orcid.org/0000-0003-0162-2277>

Mega Fatimah Rosana  <https://orcid.org/0000-0003-3741-6926>

REFERENCES

- Abedini, A., Khosravi, M. & Dill, H.G. (2020) Rare earth element geochemical characteristics of the late Permian Badamlu karst bauxite deposit, NW Iran. *Journal of African Earth Sciences*, 172(August), 103974. Available from: <https://doi.org/10.1016/j.jafrearsci.2020.103974>
- Balaram, V. (2019) Rare earth elements: a review of applications, occurrence, exploration, analysis, recycling, and environmental impact. *Geoscience Frontiers*, 10(4), 1285–1303. Available from: <https://doi.org/10.1016/j.gsf.2018.12.005>
- Berger, A., Janots, E., Gnos, E., Frei, R. & Bernier, F. (2014) Rare earth element mineralogy and geochemistry in a laterite profile from Madagascar. *Applied Geochemistry*, 41, 218–228. Available from: <https://doi.org/10.1016/j.apgeochem.2013.12.013>
- Borst, A.M., Smith, M.P., Finch, A.A., Estrade, G., Villanova-de-Benavent, C., Nason, P. et al. (2020) Adsorption of rare earth elements in regolith-hosted clay deposits. *Nature Communications*, 11(1), 1–15. Available from: <https://doi.org/10.1038/s41467-020-17801-5>
- Braun, J.J., Riotte, J., Battacharya, S., Violette, A., Oliva, P., Prunier, J. et al. (2018) REY-Th-U dynamics in the critical zone: combined influence of reactive bedrock accessory minerals, Authigenic phases, and hydrological sorting (mule hole watershed, South India). *Geochemistry, Geophysics, Geosystems*, 19(5), 1611–1635. Available from: <https://doi.org/10.1029/2018GC007453>
- Chapela Lara, M., Buss, H.L. & Pett-Ridge, J.C. (2018) The effects of lithology on trace element and REE behavior during tropical weathering. *Chemical Geology*, 500(September), 88–102. Available from: <https://doi.org/10.1016/j.chemgeo.2018.09.024>
- Chen, Z. (2011) Global rare earth resources and scenarios of future rare earth industry. *Journal of Rare Earths*, 29(1), 1–6. Available from: [https://doi.org/10.1016/S1002-0721\(10\)60401-2](https://doi.org/10.1016/S1002-0721(10)60401-2)
- Cobbing, E.J. (2005) Granites. In: Barber, A.J., Crow, M.J. & Milsom, J.S. (Eds.) *Geological Society, London:Amsterdam: Memoirs*, Vol. 31. pp. 54–62. Available from: <https://doi.org/10.1144/GSL.MEM.2005.031.01.05>
- Duzgoren-Aydin, N.S. & Aydin, A. (2009) Distribution of rare earth elements and oxyhydroxide phases within a weathered felsic igneous profile in Hong Kong. *Journal of Asian Earth Sciences*, 34(1), 1–9. Available from: <https://doi.org/10.1016/j.jseaes.2008.03.010>
- Fu, W., Li, X., Feng, Y., Feng, M., Peng, Z., Yu, H. et al. (2019) Chemical weathering of S-type granite and formation of rare earth element (REE)-rich regolith in South China: critical control of lithology. *Chemical Geology*, 520(12), 33–51. Available from: <https://doi.org/10.1016/j.chemgeo.2019.05.006>
- Giovannini, A.L., Bastos Neto, A.C., Porto, C.G., Takehara, L., Pereira, V.P. & Bidone, M.H. (2021) REE mineralization (primary, supergene and sedimentary) associated to the Morro dos Seis Lagos Nb (REE, Ti) deposit (Amazonas, Brazil). *Ore Geology Reviews*, 137(June), 104308. Available from: <https://doi.org/10.1016/j.oregeorev.2021.104308>
- Huang, J., He, H., Tan, W., Liang, X., Ma, L., Wang, Y. et al. (2021a) Groundwater controls REE mineralisation in the regolith of South China. *Chemical Geology*, 577(April), 120295. Available from: <https://doi.org/10.1016/j.chemgeo.2021.120295>
- Huang, J., Tan, W., Liang, X., He, H., Ma, L., Bao, Z. et al. (2021b) REE fractionation controlled by REE speciation during formation of the Renju regolith-hosted REE deposits in Guangdong Province, South China. *Ore Geology Reviews*, 134(November 2020), 104172. Available from: <https://doi.org/10.1016/j.oregeorev.2021.104172>
- Ishihara, S. & Murakami, H. (2006) Fractionated ilmenite-series granites in southwest Japan: source magma for REE-Sn-W mineralizations. *Resource Geology*, 56(3), 245–256. Available from: <https://doi.org/10.1111/j.1751-3928.2006.tb00282.x>
- Li, M.Y.H. & Zhou, M.-F. (2020) The role of clay minerals in formation of the regolith-hosted heavy rare earth element deposits. *American Mineralogist*, 105(1), 92–108. Available from: <https://doi.org/10.2138/am-2020-7061>
- Liu, S.L., Fan, H.R., Liu, X., Meng, J., Butcher, A.R., Yann, L. et al. (2023) Global rare earth elements projects: new developments and supply chains. *Ore Geology Reviews*, 157(March), 105428. Available from: <https://doi.org/10.1016/j.oregeorev.2023.105428>
- Louvel, M., Etschmann, B., Guan, Q., Testemale, D. & Brugger, J. (2022) Carbonate complexation enhances hydrothermal transport of rare earth elements in alkaline fluids. *Nature Communications*, 13(1), 1–11. Available from: <https://doi.org/10.1038/s41467-022-28943-z>
- McDonough, W.F. & Sun, S.S. (1995) The composition of the earth. *Chemical Geology*, 120, 223–253.
- Mellor, A. & Wilson, M.J. (1989) Origin and significance of Gibbsite montane soils in Scotland, U.K. *Arctic and Alpine Research*, 21(4), 417–424. Available from: <https://doi.org/10.2307/1551650>
- Miyawaki, R. & Nakai, I. (1996) Crystal chemical aspects of rare earth minerals. In: Johens, A.P., Wall, F. & Williams, C.T. (Eds.) *Rare earth minerals, chemistry, origin and ore deposits, mineralogical society series*, 7. London: Chapman & Hall, pp. 21–40.
- Mukai, H., Kon, Y., Sanematsu, K., Takahashi, Y. & Ito, M. (2020) Microscopic analyses of weathered granite in ion-adsorption rare earth deposit of Jianxi Province, China. *Scientific Reports*, 10(1), 1–11. Available from: <https://doi.org/10.1038/s41598-020-76981-8>
- Nesbitt, H. (1979) Mobility and fractionation of REE during weathering of a granodiorite. *Nature*, 279, 206–210.
- Ng, S.W.P., Whitehouse, M.J., Roselee, M.H., Teschner, C., Murtadha, S., Oliver, G.J.H. et al. (2017) Late Triassic granites from Bangka, Indonesia: a continuation of the main range granite province of the South-east Asian Tin Belt. *Journal of Asian Earth Sciences*, 138, 548–561. Available from: <https://doi.org/10.1016/j.jseaes.2017.03.002>
- Nugraheni, R.D., Sunjaya, D. & Burhannuddin, M. (2020) The enrichment mechanism of rare earth elements in weathered granitoids, tin placer and bauxite laterite. *International Journal of Scientific and Technology Research*, 9(3), 1506–1511.
- Oktaviani, A.D., Dewi, D.K. & Sihombing, F.M.H. (2021) Structural control of primary tin mineralization (case study: Parit Tiga, West Bangka regency, Bangka Belitung). *IOP Conference Series: Geology Reviews*, 137(June), 104308. Available from: <https://doi.org/10.1016/j.oregeorev.2021.104308>

- Earth and Environmental Science*, 830(1), 12046. Available from: <https://doi.org/10.1088/1755-1315/830/1/012046>
- Radusinovi, S., Jelenkovi, R., Pa, A., Simi, V., Bo, D., Holclajtner-antunovi, I. et al. (2017) Content and mode of occurrences of rare earth elements in the Zagrad karstic bauxite deposit (Nikšić area, Montenegro), 80, 406–428. Available from: <https://doi.org/10.1016/j.joregeorev.2016.05.026>
- Sager, M. & Wiche, O. (2024) Rare earth elements (REE): origins, dispersion, and environmental implications—a comprehensive review. *Environments*, 11(2), 24. Available from: <https://doi.org/10.3390/environments11020024>
- Sanematsu, K. & Watanabe, Y. (2016) Characteristics and genesis of ion adsorption-type rare earth element deposits. In: *Rare earth and critical elements in ore deposits*. Littleton, CO: Society of Economic Geologists. Available from: <https://doi.org/10.5382/rev.18.03>
- Sanematsu, K., Murakami, H., Watanabe, Y., Duangsurigna, S. & Vilayhack, S. (2009) Enrichment of rare earth elements (REE) in granitic rocks and their weathered crusts in central and southern Laos. *Bulletin of the Geological Survey of Japan*, 60, 527–558.
- Sanematsu, K., Kon, Y., Imai, A., Watanabe, K. & Watanabe, Y. (2013) Geochemical and mineralogical characteristics of ion-adsorption type REE mineralization in Phuket, Thailand. *Mineralium Deposita*, 48(4), 437–451. Available from: <https://doi.org/10.1007/s00126-011-0380-5>
- Sanematsu, K., Kon, Y. & Imai, A. (2015) Influence of phosphate on mobility and adsorption of REEs during weathering of granites in Thailand. *Journal of Asian Earth Sciences*, 111, 14–30. Available from: <https://doi.org/10.1016/j.jseae.2015.05.018>
- Santana, I.V., Wall, F. & Botelho, N.F. (2015) Occurrence and behavior of monazite-(Ce) and xenotime-(Y) in detrital and saprolitic environments related to the Serra Dourada granite, Goiás/Tocantins state, Brazil: potential for REE deposits. *Journal of Geochemical Exploration*, 155, 1–13. Available from: <https://doi.org/10.1016/j.jgexplo.2015.03.007>
- Santos, J.C.B.d., Le Pera, E., Oliveira, C.S.d., Souza Júnior, V.S.d., Pedron, F.d.A., Corrêa, M.M. et al. (2019) Impact of weathering on REE distribution in soil-saprolite profiles developed on orthogneisses in Borborema Province, NE Brazil. *Geoderma*, 347(April), 103–117. Available from: <https://doi.org/10.1016/j.geoderma.2019.03.040>
- Schmandt, D.S., Cook, N.J., Ciobanu, C.L., Ehrig, K., Wade, B.P., Gilbert, S. et al. (2017) Rare earth element fluorocarbonate minerals from the olympic dam Cu-U-Au-Ag deposit, South Australia. *Minerals*, 7(10), 202. Available from: <https://doi.org/10.3390/min7100202>
- Schoonheydt, R.A. & Johnston, C.T. (2013) Chapter 5—Surface and Interface chemistry of clay minerals. In: Bergaya, F. & Lagaly, G. (Eds.) *Handbook of clay science*, Vol. 5. Elsevier. Amsterdam, pp. 139–172. Available from: <https://doi.org/10.1016/B978-0-08-098258-8.00005-5>
- Schwartz, M.O., Rajah, S.S., Askury, A.K., Putthapiban, P. & Djaswadi, S. (1995) The southeast Asian tin belt. *Earth Science Reviews*, 38(2–4), 95–293. Available from: [https://doi.org/10.1016/0012-8252\(95\)00004-T](https://doi.org/10.1016/0012-8252(95)00004-T)
- Sharma, R. & Srivastava, P.K. (2014) Hydrothermal fluids of magmatic origin. *Modelling of Magmatic and Allied Processes*, 9, 181–208. Available from: https://doi.org/10.1007/978-3-319-06471-0_9
- Supandjono, U., Margono, R. & Partoyo, E. (1995) *Geological map of the south Bangka sheet, Sumatera*. Bandung: Geological Research and Development Center.
- Tampubolon, A., Syafri, I., Rosana, M.F. & Yuningsih, E.T. (2022) The occurrence of primary REE minerals and their Para genesis within S-type granite and quartz vein, South Bangka, Bangka Belitung Islands, Indonesia. *Journal of Electrical Electronics Engineering*, 1, 64–8. Available from: <https://doi.org/10.33140/jee.01.01.06>
- Teitler, Y., Cathelineau, M., Ulrich, M., Ambrosi, J. P., Munoz, M., & Sevin, B. (2019). Petrology and geochemistry of scandium in New Caledonian Ni-Co laterites. *Journal of Geochemical Exploration*, 196, 131–155. <https://doi.org/10.1016/j.jgexplo.2018.10.009>
- Torrent, J. & Benayas, J. (1977) Origin of gibbsite in a weathering profile from granite in west-central Spain. *Geoderma*, 19(1), 37–49. Available from: [https://doi.org/10.1016/0016-7061\(77\)90012-X](https://doi.org/10.1016/0016-7061(77)90012-X)
- U. S. Department of Energy. (2023) *Critical Materials Assessment, July*. Washington, D.C: U. S. Department of Energy, p. 240.
- Voncken, J.H.L. (2016). The Rare Earth Elements. In *Journal of the American Chemical Society* (Vol. 86(21), 4739). Springer International Publishing. <https://doi.org/10.1007/978-3-319-26809-5>
- Wang, Z.-Y., Fan, H.-R., Zhou, L., Yang, K.-F. & She, H.-D. (2020) Carbonatite-related REE deposits: an overview. *Minerals*, 10(11), 965. Available from: <https://doi.org/10.3390/min10110965>
- Wilke, B.-M. & Schwertmann, U. (1977) Gibbsite and halloysite decomposition in strongly acid podzolic soils developed from granitic saprolite of the Bayerischer Wald. *Geoderma*, 19(1), 51–61. Available from: [https://doi.org/10.1016/0016-7061\(77\)90013-1](https://doi.org/10.1016/0016-7061(77)90013-1)
- Xing, J., Jiang, Y., Xian, H., Yang, W., Yang, Y., Tan, W. et al. (2023) Hydrothermal alteration and the remobilization of rare earth elements during reprecipitation of nano-scale apatite in phosphorites. *Lithos*, 444–445(July 2022), 107113. Available from: <https://doi.org/10.1016/j.lithos.2023.107113>
- Xu, C., Kynický, J., Smith, M.P., Kopriva, A., Brtnický, M., Urubek, T. et al. (2017) Origin of heavy rare earth mineralization in South China. *Nature Communications*, 8, 14598. Available from: <https://doi.org/10.1038/ncomms14598>
- Yusoff, Z.M., Ngwenya, B.T. & Parsons, I. (2013) Mobility and fractionation of REEs during deep weathering of geochemically contrasting granites in a tropical setting, Malaysia. *Chemical Geology*, 349–350, 71–86. Available from: <https://doi.org/10.1016/j.chemgeo.2013.04.016>
- Zhao, X., Rangel Guillen, T., Graham, T.R., Chen, P., Zhao, Y., Mergelsberg, S.T. et al. (2024) Incorporation of rare earth elements Sc, Y and La into gibbsite. *Chemical Engineering Journal*, 485(October 2023), 149809. Available from: <https://doi.org/10.1016/j.cej.2024.149809>

How to cite this article: Agung, Y.Z., Watanabe, Y., Tampubolon, A., Purnama, A.B. & Rosana, M. F. (2024) Characteristics of REE enrichments in the weathered granitic crust, Toboali, South Bangka: Possibility for ion adsorption-type REE mineralization. *Resource Geology*, 74(1), e12343. Available from: <https://doi.org/10.1111/rge.12343>